ACS APPLIED MATERIALS & INTERFACES

Research Article

www.acsami.org

Liquid Phase Deposition of a Space-Durable, Antistatic SnO_2 Coating on Kapton

Katya Gotlib-Vainstein,[†] Irina Gouzman,[‡] Olga Girshevitz,[†] Asaf Bolker,[‡] Nurit Atar,[‡] Eitan Grossman,[‡] and Chaim N. Sukenik*,[†]

[†]Department of Chemistry and Institute for Nanotechnology and Advanced Materials, Bar-Ilan University, Ramat Gan, Israel 52900

[‡]Space Environment Department, Soreq NRC, Yavne 81800, Israel

ABSTRACT: Polyimides are widely used in thermal blankets covering the external surfaces of spacecrafts due to their space durability and their thermo-optical properties. However, they are susceptible to atomic oxygen (AO) erosion, the main hazard of low Earth orbit (LEO), and to electrical charging. This work demonstrates that liquid phase deposition (LPD) of 100 nm of tin oxide creates a protective coating on Kapton polyimide that has good adherence and is effective in preventing AO-induced surface erosion and in reducing electrical charging. The as-deposited tin oxide induces no significant changes in the original thermo-optical properties of the polymer and is effective in preventing electrostatic discharge (ESD). The durability of the oxide coating under AO attack was studied using oxygen RF plasma. The AO exposure did not result in any significant changes in surface morphology, thermo-optical, mechanical, and electrical properties of the tin oxide-coated Kapton. The erosion yield of tin oxide-coated Kapton was negligible after exposure to 6.4×10^{20} O atoms·cm^{-2} of LEO equivalent AO fluence, indicating a complete protection of Kapton by the LPD deposited coating. Moreover, the tin oxide coating is flexible enough so that its electrical conductivity stays within the desired range of antistatic materials despite mechanical manipulations. The advantages of liquid phase deposited oxides in terms of their not being line of site limited are well established. We now extend these advantages to coatings that reduce electrostatic discharge while still providing a high level of protection from AO erosion.

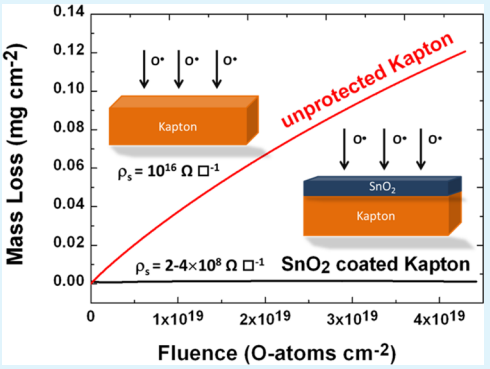

KEYWORDS: *atomic oxygen, space environment, tin oxide, liquid phase deposition, electrostatic discharge*

1. INTRODUCTION

Deployable structures and ultra-lightweight spacecraft require polymeric materials that possess a unique combination of mechanical and thermo-optical properties.[1] Polyimides like Kapton are very attractive for these applications because they are lightweight and flexible, with good wear and thermo-optical properties.[2] Kapton, which is used as an external layer of a multilayer isolation system,[3] is exposed extensively to the space environment. The low Earth orbit environment (LEO) introduces different hazards to external spacecraft materials, such as exposure to atomic oxygen (AO), UV and ionizing radiation, micrometeoroids, orbital debris, and charged particle bombardment.[4−6] It is well-known that AO can cause significant erosion of Kapton;[7,8] e.g., a 25 μm thick Kapton blanket would completely erode within 6 months in LEO.[7] Thus, structures in the LEO environment require protective coatings.

Various approaches have been developed to mitigate the AO erosion of polyimides. The protective strategies may be divided into three categories: (a) protective coatings, mainly metal oxides, produced by different methods;[7,9,10] (b) surface modification, such as ion implantation or direct application of siloxanes;[11−13] (c) development of advanced hybrid materials that are stable in an oxidative environment, e.g., POSS/polyimide nanocomposites.[14−16]

Avoiding or minimizing charging is an important consideration in the design of spacecraft. Energetic charged particles can penetrate a near surface polymer layer, thus depositing a charge onto insulating materials. This can result in electrostatic charge (ESC) build-up, development of large electric fields, and eventually a discharge.[17,18] Electrostatic discharge (ESD) can cause serious damage to delicate spacecraft electronics.[19] The surface resistivity needed to mitigate ESC build-up on insulators is in the range of 10^6 to 10^{10} Ω □$^{-1}$.[20] The widely used SiO_2 protective coating physically blocks the interaction with AO[21] but does not prevent the ESC build-up due to its insulating properties. Indium tin oxide is a standard conductive coating;[22] however, it is very brittle and loses its conductivity when folded to the point of cracking.[23] The combination of sufficient electrical conductivity to diminish ESC build-up without affecting material flexibility is difficult to achieve.

Liquid phase deposition (LPD) is a commonly used method for preparing oxide ceramic films. It is technologically simple

Received: October 21, 2014
Accepted: January 21, 2015
Published: January 21, 2015

DOI: 10.1021/am5072817
ACS Appl. Mater. Interfaces 2015, 7, 3539−3546

since it involves film deposition from aqueous solution under near-ambient conditions and allows coatings of substrates with complex shapes.[24] In previously published work, we demonstrated that a titania (TiO_2) coating provides good protection of Kapton against AO (mass loss about 1% compared to uncoated Kapton).[25] However, the cracking of the coating and its high resistivity renders a TiO_2 coating unsatisfactory for applications where preventing ESD is critical. The present work demonstrates that LPD tin oxide (SnO_2) overcomes both of these drawbacks.

In this work, we extend the previously reported LPD of SnO_2 films on substrates like silicon, glass, and gold electrodes,[26−28] to coating Kapton. SnO_2-coated Kapton is characterized in terms of its morphology, growth rate, chemical composition, mechanical and thermo-optical properties, as well as AO durability. We also compare the electrical properties of the previously reported TiO_2-coated Kapton with those of SnO_2-coated Kapton by Kelvin probe atomic force microscopy (KP-AFM), and electrical measurements. We also use Rutherford backscattering spectrometry (RBS) and the distortions in these spectra created by ion beam induced charging to compare variously treated Kapton films with each other and with simulated data so as to demonstrate the effectiveness of SnO_2 as a dissipative coating.

2. EXPERIMENTAL SECTION

2.1. Thin Film Preparation. TiO_2 and SnO_2 coatings were prepared on 125 μm thick Kapton 500 HN sheets (DuPont) by LPD.[24−26] Prior to coating, the as-received sheets were cut into 1 cm × 1 cm squares or 1 cm × 4 cm rectangular coupons, washed with double distilled water and ethanol, and dried under nitrogen. The coupons were pretreated by exposing them to an air plasma (Harrick, model PDC-3XG) at a pressure of 0.3 mmHg and 18 W power for 20 min.[25,29,30] Immediately after plasma pretreatment, the samples were placed into the LPD solution at room temperature. The following solutions were used

(i) TiO_2: 0.3 M H_3BO_3 and 0.1 M $(NH_4)_2TiF_6$ in water. Substrates were left in the solution for 8 h.

(ii) SnO_2: 0.03 M SnF_2, 0.45 M H_3BO_3, 0.15 M HF, and 0.06 M H_2O_2 in water. The deposition time varied from 1 to 6 h.

The coated samples were rinsed in water and methanol before drying under conditions of controlled humidity[29] for 53 h. The stability of the coating was confirmed by sonication in water for 10 min. The robustness and good adhesion of the coating were tested. All the SnO_2−coated samples were found to be stable to sonication in water for 10 min and were sufficiently adherent so that they were not compromised by a standard tape test.[31]

2.2. Characterization Techniques. *2.2.1. Scanning Electron Microscopy (SEM).* The surface morphology of the samples was assessed by SEM (Magellan, FEI), at an accelerating voltage in the range of 5−10 kV with a 10 nm surface gold coating.

2.2.2. X-ray Photoelectron Spectroscopy (XPS). Surface chemical composition was determined by XPS (Kratos AXIS-HS spectrometer) using a monochromatized Al Kα source. All data acquisition was done in a hybrid mode (using electrostatic and magnetic lenses) and detection pass energies of 40−80 eV. All XPS measurements were carried out at room temperature, under pressure in the range of 1.0−3.0 × 10^{-9} Torr. The spectra were acquired with an electron flood gun for charge neutralization. The spectrometer energy scale was calibrated according to the ISO TC/201 SC7 international procedure for binding energy (BE) calibration with Au $4f_{7/2}$ = 83.98 eV and Cu $2p_{3/2}$ = 932.67 eV. Data processing was done with VISION 2.1 software (Kratos) using sensitivity factors for quantification. In most cases a Shirley background was used.[32] Curve fitting was performed using a 80/20 Gaussian/Lorentzian line shape.

2.2.3. Rutherford Backscattering Spectrometry (RBS). The thickness of the SnO_2 layers was measured by RBS, using SnO_2 atomic density. RBS was also used for comparing the charging of uncoated Kapton and Kapton coated with TiO_2 or SnO_2 films. This work was done using a 1.7 MV Pelletron accelerator (NEC, USA). All spectra were collected using a 2.023 MeV $^4He^+$ ± 1 keV beam. The beam current was ∼10 nA, with a nominal beam diameter of 1.5 mm. An electron suppressor between the beam entrance and the sample holder was biased at 100 V vs ground. A second electron suppressor was placed in front of the sample, and it was biased at −300 V relative to the sample holder. RBS spectra were acquired using a fixed silicon drift detector (ULTRA Silicon-Charged Particle Detector, ORTEC) in a Cornell geometry with detector scattering angle 169° and solid angle of 2.7 msr. A normal incident beam was used for all measurements. All samples were mounted on the holder by double sided, self-adhesive carbon tape. In the case of film thickness studies, the charging effect on oxide-coated Kapton samples was compensated by a thin Au coating (8 nm). Data Furnace computation code (NDFv9.6a program)[33] and SRIM 2003[34] stopping powers were used to fit the data.

2.2.4. Atomic Force Microscopy (AFM). All scanning probe microscopy measurements were performed using an ICON instrument (Bruker AXS SAS). The measurements were carried out in tapping, nanoindentation/scratching and surface potential modes. The root-mean-square roughness (R_q) was calculated from 1 × 1 μm^2 micrographs. The deflection sensitivity of each probe was measured by pressing the probe on a hard surface, and the spring constant was calibrated by the "Sader method".[35] Nanoscratching was done using a diamond coated tip (DDESP) (force constant of 20−80 N m^{-1}, Digital Instruments, Santa Barbara, CA). Nanoscratching was done with the indenter at variable normal loads of 10−20 μN, a sliding speed of 0.3 $\mu m\ s^{-1}$, and a scratch length of ∼1.5 μm. Nanoindentation was done with a Berkovich probe (force constant of 194 N m^{-1}) with applied load of 5 μN. The stiffness value was calculated based on 18 points of indentation for each sample. The same indenter was used to image the area after the nanomechanical tests. The electrical measurements were done using scanning Kelvin Probe AFM under ambient conditions. The surface potential was determined using conductive probes coated with cobalt/chromium (MESP; force constant of 1−5 N m^{-1}, Digital Instruments, Santa Barbara, CA). The lift scan height was adjusted to 50 nm, and the applied voltage on the tip was 1 V. Before analysis of the images, first order "flatten" and "planefit" functions were applied to each image. The roughness was determined by Nanoscope analysis software.

2.2.5. Thermo-Optical Measurements. Solar absorptance (α_s) and thermal emittance (ε) were measured using a TASA 2000 portable reflectometer (AZ Technology, Inc.).

2.2.6. Surface Resistivity. Macroscopic electrical properties of the samples in the lateral direction were measured using a source meter (Keithly 2400), under ambient conditions. In order to determine sheet resistivity, a set of parallel electrodes was applied across the surface of a 0.5 × 4 cm^2 sample to form several square segments with area of about 25 mm^2 each. The sheet resistance, R, was measured for different areas with a constant width (5 mm), w, and increasing length, L (up to 4 cm). The sheet resistivity, ρ_s, in units of $\Omega\ \square^{-1}$ (ohm per a single square segment) is related to the sheet resistance according to the relationship:

$$R = \rho_s \frac{L}{w} \tag{1}$$

ρ_s was calculated as the slope of the linear trend line that was fitted to the resistance versus the number of measured segments, L/w, and the contact resistance is expressed by the intercept of the linear line with the y axis.

2.3. Atomic Oxygen Exposure. The AO exposure facility is based on a LB-3000 Advanced Energy RF-plasma system with a feed gas of 99.999% pure oxygen. The system was operated at a pressure of 40 mTorr, power of 1000 W, and oxygen flow of 10 sccm. Redirection of the afterglow through right angle deflection results in a strong reduction of ion current and UV radiation flux, facilitated by a supply of electrons from the metallic chamber walls, and radiation absorption

DOI: 10.1021/am5072817
ACS Appl. Mater. Interfaces 2015, 7, 3539−3546

by the walls, respectively. The afterglow was characterized by optical emission spectroscopy, electrical measurements, UV radiation measurements, and Kapton etching rate measurements. A detailed description of the AO simulation system is presented elsewhere.[36] In the present work, the samples were exposed using two exposure regimes. In the first regime (regime I), special care was taken to expose the samples predominantly to AO atoms, without electron and ion fluxes originated from RF plasma. The LEO equivalent AO flux in this case is low, about 5×10^{13} atoms $s^{-1}cm^{-2}$. Relatively low LEO equivalent AO fluence (about 4.3×10^{19} atoms cm^{-2}) was achieved using this regime, and it was used for continuous online monitoring of mass losses from uncoated and SnO_2-coated samples. To increase AO flux, the experiment was carried out under severe exposure conditions (regime II), using a direct RF O_2 plasma afterglow. The LEO equivalent AO flux in this experiment was 6.18×10^{15} atoms s^{-1} cm^{-2} and the total AO fluence was 6.4×10^{20} atoms cm^{-2}.

Atomic oxygen fluence measurements were conducted based on Kapton-HN mass loss, assuming an erosion yield of 2.80×10^{-24} cm^3·O $atom^{-1}$ and Kapton HN density of 1.42 g cm^{-3}.[37] The erosion yield was determined gravimetrically, using an analytical balance (Sartorius SE2) with an accuracy of ±0.1 μg. All the measurements were carried out immediately after sample removal from the exposure facility. The time of sample exposure to ambient air did not exceed 2 min.

For measuring the kinetics of mass loss, polyimide films were spin-coated onto quartz crystal microbalance (QCM) crystals using a Dupont procedure for deposition of polyimide (Pyralin PI 2545, HD MicroSystems; 4−5 μm thick).[38] The deposited polyimide films were shown to be similar to Kapton HN films based on their FTIR spectra.[39] SnO_2 coatings were deposited on Pyralin-coated QCM crystals, using the same protocol as had been applied to the Kapton sheets.

3. RESULTS AND DISCUSSION

3.1. SnO_2 Coated Kapton. *3.1.1. Growth Rate and Surface Morphology.* Commercial Kapton was coated with uniform, adherent, amorphous SnO_2 by LPD. Air plasma pretreatment of the Kapton samples was needed to ensure good adhesion of the SnO_2 to the Kapton. The $[SnF_6]^{-2}$ complex that is necessary for LPD was prepared in situ by reacting SnF_2 with H_2O_2 in the presence of HF. An overall ratio of F/Sn = 7 in solution is favorable for creating a uniform, crack-free (by HRSEM), oxide film on the Kapton surface. Figure 1 shows HRSEM and AFM images of the SnO_2 coating on Kapton obtained after 6 h of LPD. Both the HR-SEM and the AFM confirm that we obtain good surface coverage. Surface roughness, estimated by AFM, is about R_q = 4.7 nm, a little over 3 nm rougher than the original plasma treated Kapton (1.5 nm). This additional roughness is negligible relative to the overall thickness of the deposited oxide films.

The thickness of SnO_2 films as a function of the deposition time was evaluated by RBS. Figure 2a shows RBS spectra (only the tin region is shown) measured for SnO_2-coated Kapton after different deposition times. The width of the RBS peak (full width of half-maximum) was used to calculate the film thickness.[40] A minimum deposition time of about 2 h was required to create a fully covered surface. Increasing deposition time in the 2−6 h range results in a linear growth of the SnO_2 thickness. The short deposition time (0−2 h) deviated from the linear behavior (Figure 2b).

The slower growth rate at the beginning of the deposition process is consistent with a film growth mechanism involving solution phase nucleation. This has been previously reported for titania deposition.[41] Such a process is easy to control and provides predictable film thicknesses.

3.1.2. Atomic Oxygen Durability. SnO_2 deposited on a Pyralin-coated QCM crystal was subjected to AO exposure

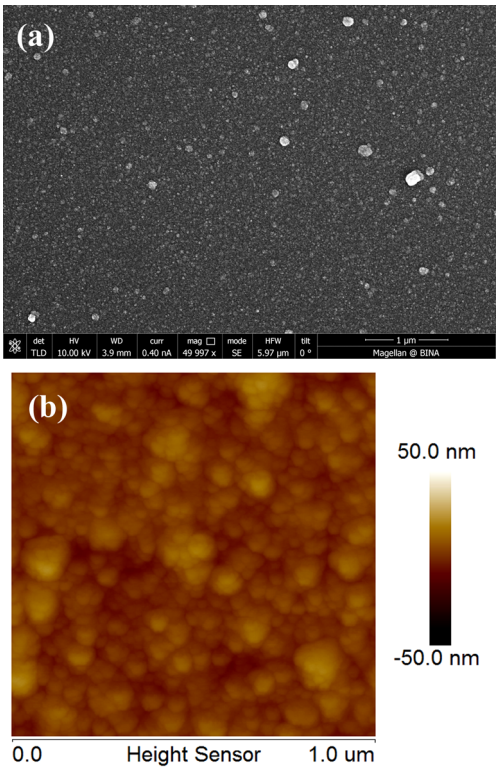

Figure 1. Representative HR-SEM (a) and AFM (b) images of SnO_2 coatings (after 6 h coating time) on Kapton.

(regime 1). The total AO fluence was 4.3×10^{19} atoms cm^{-2}. This fluence is equivalent to exposure of a satellite external surface to the LEO environment for about 2 months in an orbit of 500 km in the ram direction. Figure 3 shows mass loss measurements of two samples with different thicknesses of SnO_2 coatings (70 and 100 nm) as a function of LEO equivalent AO fluence. Both SnO_2 films, 70 and 100 nm, provide barrier layers that protect polyimide from AO. However, the 70 nm film, despite providing a fully covered surface, showed measurable mass loss (15% of unprotected Pyralin after exposure to a fluence of 4.3×10^{19} atoms cm^{-2}). Thicker, 100 nm, SnO_2 films provided complete protection against AO (Figure 3).

In a different experiment, the erosion of SnO_2-coated Kapton was measured gravimetrically after exposure to a higher fluence of 6.4×10^{20} atoms cm^{-2} using the severe exposure conditions (regime II). This fluence is equivalent to exposure of a satellite external surface to the LEO environment for about 2 years in an orbit of 500 km in the ram direction. Even under these conditions, practically no erosion of tin oxide-coated (100 nm) Kapton was observed; the erosion yield of SnO_2-coated Kapton is 0.3% of that measured for uncoated Kapton. According to our previous work,[42,43] we can confidently assume that SnO_2-coated Kapton will be durable under exposure to much higher AO fluences (in the range of 10^{21} atoms cm^{-2}) in LEO environment, or under exposure to hyperthermal AO using a Laser detonation source.[44]

The surface morphology of the AO exposed SnO_2-coated samples was measured by electron microscopy. HR-SEM showed that as deposited 70 and 100 nm SnO_2 coatings on Kapton are uniform and crack-free (as seen in Figure 1a). While the thicker coating remained crack-free and showed no morphological changes after AO exposure, the 70 nm SnO_2 film

DOI: 10.1021/am5072817
ACS Appl. Mater. Interfaces 2015, 7, 3539−3546

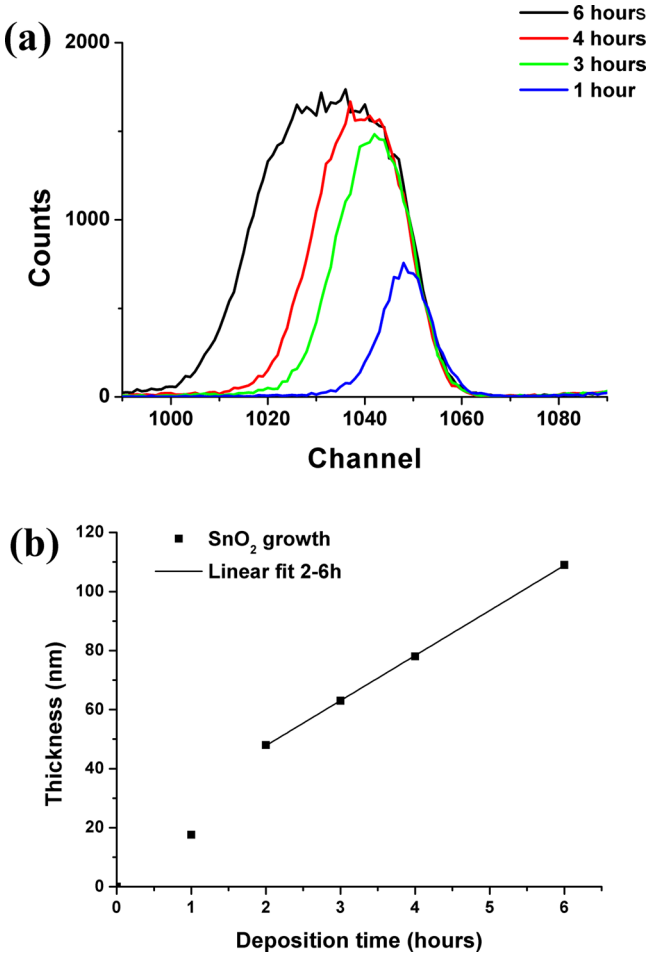

Figure 2. (a) SnO_2 peak in the RBS at various deposition times; (b) SnO_2 film thickness as a function of the deposition time, derived from RBS measurements.

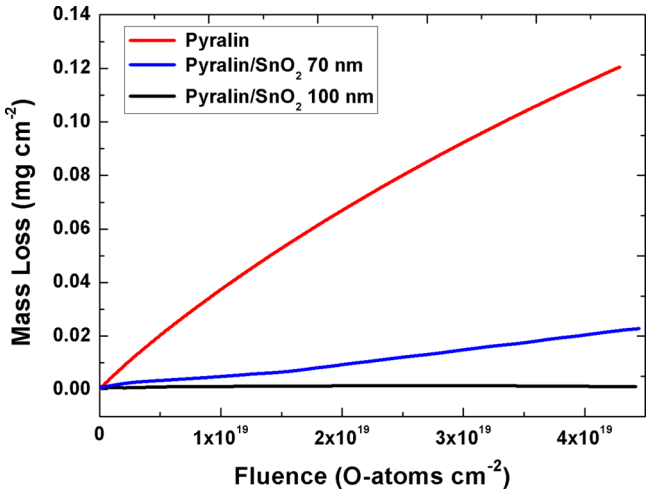

Figure 3. Pyralin and SnO_2-coated (70 and 100 nm) Pyralin mass losses as a function of AO fluence.

showed minor cracking (<1%). Those cracks (approximately 50 nm wide) are likely responsible, at least in part, for the observed mass loss. No prominent undercutting of Kapton was observed in the cracked regions; in contrast to the substantial cracking of TiO_2-coating and undercutting of Kapton that was reported previously.[25,45] The seemingly lower protection efficiency of the thinner coating (70 nm) might be due, at least in part, to diffusion of AO through the oxide layer. Further experimentation would be needed to precisely define the optimal thickness of such coatings and to sort out the details of the factors that may contribute to the need for a minimal thickness. Nevertheless, the observation that 100 nm provides good protection is secure.

The 100 nm SnO_2-coated Kapton, before and after AO exposure, was studied by XPS. The quantitative analysis of surface composition was carried out using the detailed XPS scans of C1s, O1s, and $Sn3d_{5/2}$ and standard atomic photoionization cross-section values. The results are summarized in Table 1. As-deposited SnO_2 coating showed a

Table 1. Surface Elemental Composition (at. %) Based on XPS Analysis

	O	Sn	C	O/Sn
Kapton + SnO_2	41.3	19.4	39.4	2.1
Kapton + SnO_2 after AO	43.5	20.2	36.3	2.2

substantial concentration of carbon on the surface. However, the absence of N1s signal indicated that this carbon originated from adventitious carbon contamination of the coated surface rather than from the underlying Kapton substrate. Based on the position and the line shapes of the O1s and Sn3d peaks, it is concluded that no chemical changes occur in the SnO_2 coating after AO exposure. In both cases, the peak at 487.5 eV corresponds to Sn^{4+} and the peak at 531.5 eV corresponds to O^{2-}. The ratio of oxygen-to-tin showed minimal change, from 2.1 to 2.2. A decrease in the carbon content, and a slight increase in oxygen may be explained by losses of adventitious carbon and postexposure water adsorption, respectively.

Having ascertained that the 100 nm thickness was essential for good AO protection, all subsequent characterizations were done with samples of this thickness. This means that the mechanical, thermo-optical, and electrical measurements reported below were all done on 100 nm thick samples before and after exposure to 4.3×10^{19} atoms cm^{-2} AO fluence.

3.1.3. Mechanical Properties. The SnO_2-coated samples were scratch tested before and after AO exposure. Figure 4 shows AFM images of SnO_2-coated Kapton samples after scratching with forces of 10, 15, and 20 μN. Both samples showed visible scratch grooves at all the applied loads. However, the measured groove depth of the scratches showed some differences. The 10 μN scratch is very ill defined on the as-deposited SnO_2 with scratch depths of 10.4 and 27.1 nm for 15 and 20 μN applied loads. The AO exposed SnO_2 showed grooves of 10.3, 15.5 and 29.7 nm, for 10, 15, and 20 μN, respectively. The AO exposed samples showed slightly deeper scratch grooves. Such small changes do not suggest that the SnO_2 undergoes serious mechanical changes after AO exposure. Those changes are in the range of the roughness of the SnO_2 film (R_q = 4.7 nm). Note that SnO_2 coating improves the scratch resistance of pristine Kapton which can be scratched even with 5 μN (data not shown).[25] Thus, while these results suggest that this improved scratch resistance due to the SnO_2 coating may be somewhat undermined by the AO exposure, further work is needed to clarify this effect and its durability.

3.1.4. Thermo-Optical Properties. Thermo-optical properties, namely, solar absorptance (α_s) and thermal emittance (ε), are responsible for the passive thermal control of spacecraft components. The equilibrium temperature, T (K), of SnO_2-

DOI: 10.1021/am5072817
ACS Appl. Mater. Interfaces 2015, 7, 3539−3546

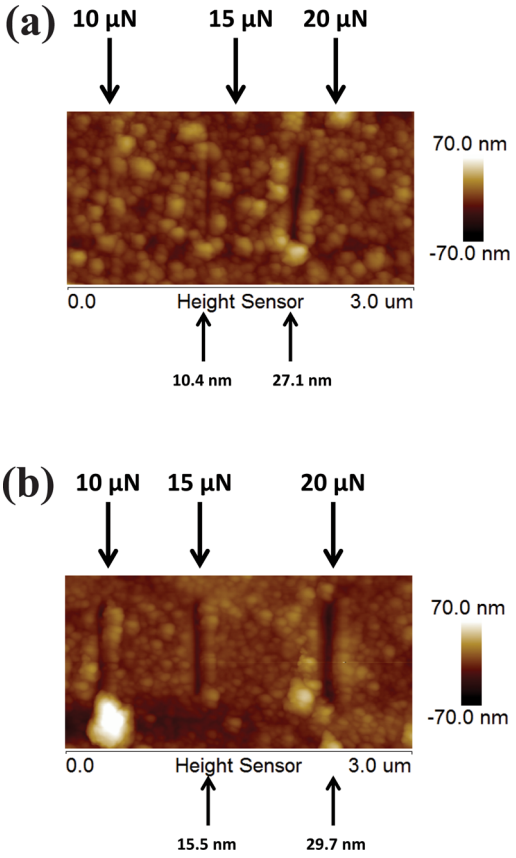

Figure 4. AFM images of scratch grooves and their depth on SnO_2-coated Kapton, before (a) and after (b) AO exposure.

coated Kapton in space is governed by the heat it absorbs from the sun and the heat it emits to its surroundings. It is calculated by[4]

$$T = \left(\frac{\alpha_s}{\varepsilon}\right)^{1/4}\left(\frac{SA_n}{\sigma A}\right)^{1/4} \quad (2)$$

where α_s is related to the film's solar absorptance, ε is its emittance, S (W m^{-2}) is the solar flux per unit area at the spacecraft orbit, A_n (m^2) is the film's surface area normal to the solar flux, A (m^2) is its total surface area, and σ (5.67×10^{-8} W m^{-2} K^{-4}) is the Stefan–Boltzmann constant. The calculated maximum temperature is related to a normal position and solar flux, S, of 1366.1 W m^{-2}, the average value above the earth's atmosphere at 1 AU distance.[46]

Thermo-optical properties of Kapton and SnO_2-coated Kapton, before and after AO exposure, are summarized in Table 2. SnO_2 coating affects the α_s/ε ratio, so that the value α_s/ε = 0.507 (for uncoated Kapton) is increased to α_s/ε = 0.763. Subsequently, the equilibrium temperature of the SnO_2-coated Kapton is increased by 35.8 °C, a reasonable temperature for a thermal blanket. The increase of the α_s/ε might be related to the slightly increased roughness of the oxide coating. After AO exposure, the α_s/ε ratio for uncoated Kapton increases from 0.507 to 0.634, while the coated sample does not show a significant change (α_s/ε = 0.778). Stable thermo-optical properties are consistent with the AO durability of the coating.

Table 2. Thermo-Optical Properties and the Equilibrium Temperature, T (K), in Space of Kapton and SnO_2-Coated Kapton, before and after AO Exposure

sample	α_s	ε	α_s/ε	T (K)
Kapton	0.426	0.840	0.507	332.4
Kapton/AO	0.538	0.850	0.634	351.6
Kapton/SnO_2	0.645	0.845	0.763	368.2
Kapton/SnO_2/AO	0.66	0.848	0.778	370.0

3.1.5. Surface Resistivity. The surface resistivity of the SnO_2-coated Kapton was measured before and after AO exposure as described above (section 2.2.6). The sheet resistivity of uncoated Kapton is about 10^{16} Ω □$^{-1}$.[47] SnO_2 coated Kapton showed a decrease of 8 orders of magnitude in surface resistivity ($\rho_s = 2 \times 10^8$ Ω □$^{-1}$). This value slightly increased after AO exposure ($\rho_s = 4 \times 10^8$ Ω □$^{-1}$); however, it stays well inside the limits for antistatic materials.[18]

This result is an important factor in recommending the potential use of SnO_2 as a barrier coating against AO. While both TiO_2 and SnO_2 have comparable capabilities in preventing AO erosion of the underlying polyimide, SnO_2 also provides a meaningful decrease in surface resistivity, thus making it an antistatic coating that can protect against ESD.

3.2. Comparison between TiO_2 and SnO_2 Coatings on Kapton. *3.2.1. Kelvin Probe AFM Measurements.* In addition to the above resistivity measurements, the electrical properties of the TiO_2 and SnO_2-coated Kapton were assessed using Kelvin probe measurements.[48] To evaluate the surface potential, half of each sample was coated with a thin (~5 nm) gold layer by sputtering; the Au coated side was used as a reference for the KP-AFM measurements. The potential images were recorded using conductive tips and a lift mode with lift height of 50 nm. The potential differences between Au and TiO_2 and between Au and SnO_2 are shown in Figure 5, panels a and b, respectively. It is important to note the different scales of the y-axes of these plots.

The potential difference between Au and TiO_2 is greater than that measured between Au and SnO_2 (61.8 vs 26.8 mV). The higher surface potential indicates a greater extent of surface charging. Those results speak to the better antistatic properties of the SnO_2 coating. This conclusion is in good agreement with previously reported electrical properties of TiO_2[49,50] and SnO_2 films.[51,52] It is also consistent with the electrical measurements reported above.

3.2.2. RBS Assessment of Surface Charging. RBS typically provides a powerful analysis method for determining surface atomic composition and elemental depth profiles.[40] When bombarding a nonconductive sample with high energy ions, there is charge accumulation on the surface. The RBS analysis of insulating materials is complicated by surface charging and spectral distortion.[53−55] A correct simulation of distorted spectra is impossible; however, we demonstrate below how we make use of spectral distortion in order to compare charge build up on a sample surface. In this way, we are not only measuring electrical properties (as described above) but are directly assessing how well a material mitigates charge build-up.

The energy of the detected backscattered particles in RBS is given by the equation

$$E_d = kE_0 \quad (3)$$

where k is the kinematic factor and E_0 is the incident energy. Due to the build-up potential φ, the incident positive He ions of charge e undergo a deceleration and strike the sample surface with the energy ($E_0 - e\varphi$). On the other hand, the backscattered particles are accelerated by the surface potential

DOI: 10.1021/am5072817
ACS Appl. Mater. Interfaces 2015, 7, 3539−3546

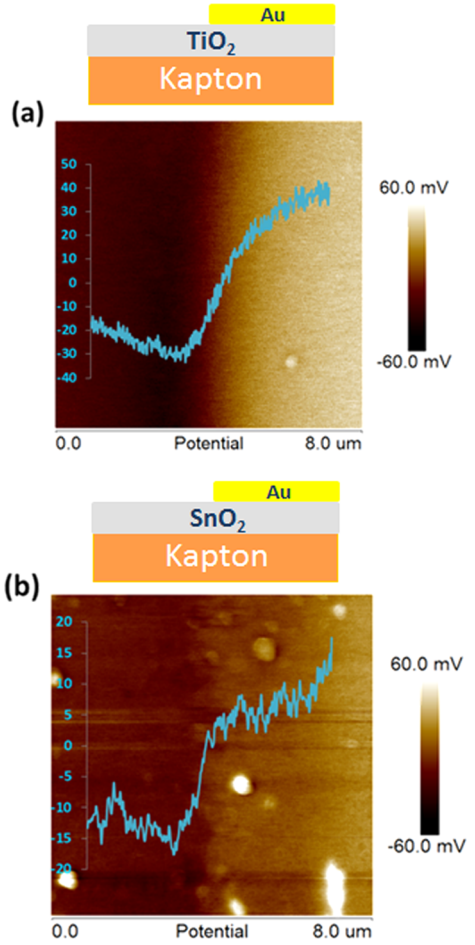

Figure 5. KP-AFM potential images of Au-TiO_2 coating (a) and Au-SnO_2 coating (b).

$ne\varphi$, where n is the He charge state +1 or +2.[56] This results in a higher detected energy for the backscattered particles from the surface.[55,57]

$$E_{d1} = k \times (E_0 - e\varphi) + ne\varphi \quad (4)$$

Therefore, the energetic shift of experimental data represents the build-up potential due to a charge accumulating effect. The surface potential of the samples can be measured as the difference between the experimental data and the simulated data, as can be seen in Figure 6.

Uncoated and oxide coated Kapton samples were irradiated with a 2.0 MeV $^4He^+$ ion beam, and the surface potential was measured as the difference between simulated and experimental data. The surface potential of Kapton was 27.5 kV. The TiO_2-coated sample had a slightly different potential, 25.1 kV. SnO_2-coating of similar thickness decreases this potential to 18.3 kV (Table 3). The lower value of surface potential observed for the SnO_2-coated sample indicates that it can be considered as coating capable of preventing electrostatic discharge.

3.3.3. Elastic Properties of TiO_2 and SnO_2 Coated Kapton. It is important to preserve the elastic properties of the Kapton after depositing the protective layer in order to allow handling of the material without degrading its electrical properties. The elastic measurements were performed on TiO_2 and SnO_2-coated Kapton by AFM nanoindentation. The stiffness of both uncoated Kapton and oxide-coated Kapton samples was estimated from nanoindentation force–displacement curves.

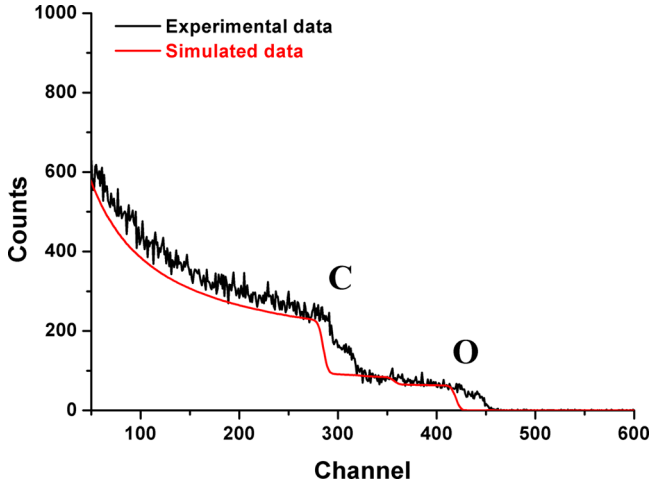

Figure 6. 2 MeV ^4He RBS spectra and simulation of pristine Kapton. Built-up potential φ was estimated by the energetic shift between experimental and simulated data.

Table 3. Surface Potential

sample	shift − ΔE (keV)	Potential − φ (kV)
Kapton	45	27.5
Kapton/TiO_2	41	25.1
Kapton/SnO_2	31	18.3

The slope of the unloading curve is the stiffness of the sample being measured.[58] The applied load was 5 μN to avoid the substrate influence on the coated samples. The Kapton stiffness was measured to be 201 ± 15 N m^{-1}, the stiffness of TiO_2-coated Kapton was 467 ± 47 N m^{-1}, and the stiffness of SnO_2-coated Kapton was 347 ± 24 N m^{-1}. Those results indicate that the SnO_2 coating is more flexible, compared to a TiO_2 coating, thus making it a better candidate for use as a protective layer.

Furthermore, the SnO_2-coated Kapton was tested to explore the effects of winding around a rod on surface resistivity. Table 4 shows the resistivity of the coated Kapton as a function of

Table 4. Effects of Windings around the Ceramic Rod on Surface Resistivity

sample	Kapton/SnO_2 as deposited	Kapton/SnO_2 after 5 windings	Kapton/SnO_2 after 10 windings
resistivity ($G\Omega\ \square^{-1}$)	0.2	3.5	21.7

windings around a ceramic rod of 2.9 mm diameter. The resistivity of the SnO_2-coated Kapton increases after 5 and 10 windings around the rod, probably due to minor migration of the oxide grains; however it did not get to the value characteristic for uncoated Kapton (10^{16} $\Omega\ \square^{-1}$).[47] This means that the coating retains its antistatic characteristics after 10 windings around the ceramic rod.[59,60]

4. CONCLUSIONS

Uniform, adherent, crack-free SnO_2 coatings with thicknesses approaching 100 nm were deposited on Kapton. The coating was characterized in terms of surface morphology, mechanical and thermo-optical properties, AO exposure durability, and chemical composition. The 100 nm thick coating was found to provide nearly complete protection of Kapton under exposure to LEO equivalent AO fluence of 6.4 × 10^{20} atoms cm^{-2}, with

DOI: 10.1021/am5072817
ACS Appl. Mater. Interfaces 2015, 7, 3539−3546

an erosion yield of only 0.3% of that measured for unprotected Kapton. No changes in chemical composition, surface morphology, scratch resistance, or thermo-optical properties were observed after AO exposure. The surface resistivity of SnO_2-coated Kapton was found to be 8 orders of magnitude lower than that of uncoated Kapton (0.2 $G\Omega\ \square^{-1}$), making it an antistatic material. The antistatic properties of SnO_2-coated Kapton were preserved even after AO exposure and after mechanical manipulations.

Charge dissipation properties of SnO_2-coated Kapton were compared to TiO_2-coated and uncoated Kapton films using Kelvin probe AFM and RBS. The surface potential of a SnO_2-coating was half that measured for a TiO_2-coating. Charging effects in RBS analyses were used to assess charge build up, and they confirm that there is less charge build up on SnO_2-coated Kapton compared with a TiO_2 coating or with uncoated Kapton.

The importance of our findings is that LPD SnO_2 can be successfully deposited on Kapton with good adhesion and that it is able to provide barrier properties that are as good or better than TiO_2 while significantly lessening the problem of ESD. Such coatings have great promise for space materials applications.

AUTHOR INFORMATION

Corresponding Author

*E-mail: chaim.sukenik@biu.ac.il.

Notes

The authors declare no competing financial interest.

ACKNOWLEDGMENTS

C.N.S. acknowledges the financial support of the Edward and Judith Stenberg Chair in Nanotechnology at Bar Ilan University. K.G. acknowledges the support of a fellowship from the Bar Ilan Institute for Nanotechnology and Advanced Materials.

REFERENCES

(1) Jenkins, C. H. M., Ed.; Gossamer Spacecraft: Membrane and Inflatable Structures Technology for Space Applications. In *Progress in Astronautics and Aeronautics.*; AIAA: Reston, VA, 2001.

(2) Miller, S. K. R.; Banks, B. Degradation of Spacecraft Materials in the Space Environment. *MRS Bull.* **2010**, *35*, 20−24.

(3) Silverman, E. M. *Space Environmental Effects on Spacecraft − LEO Material Selection Guide*; NASA Contractor Report No. 4661; Langley Research Center: Hampton, VA, 1995.

(4) Tribble, A. C. *The Space Environment: Implementation for Spacecraft Design*; Princeton University Press: Princeton, NJ, 1995.

(5) Bedingfield, K. L.; Leach, R. D.; Alexander, M. B. *Spacecraft System Failures and Anomalies Attributed to the Natural Space Environment*; NASA Reference Publication 1390, 1996.

(6) Reddy, M. R. Effect of Low Earth Orbit Atomic Oxygen on Spacecraft Materials. *J. Mater. Sci.* **1995**, *30*, 281−307.

(7) Packirisamy, S.; Schwam, D.; Litt, M. H. Atomic Oxygen Resistant Coatings for Low Earth Orbit Space Structures. *J. Mater. Sci.* **1995**, *30*, 308−320.

(8) Buczala, D. M.; Brunsvold, A. L.; Minton, T. K. Erosion of Kapton H by Hyperthermal Atomic Oxygen. *J. Spacecr. Rockets* **2006**, *43*, 421−425.

(9) Minton, T. K.; Wu, B.; Zhang, J.; Lindholm, N. F.; Abdulagatov, A. I.; O'Patchen, J.; George, S. M.; Groner, M. D. Protecting Polymers in Space with Atomic Layer Deposition Coatings. *ACS Appl. Mater. Interfaces* **2010**, *2*, 2515−2520.

(10) Zimcik, D. G.; Wertheimer, M. R.; Balmain, K. B.; Tennyson, R. C. Plasma-Deposited Protective Coatings for Spacecraft Applications. *J. Spacecr. Rockets* **1991**, *28*, 652−657.

(11) Kleiman, J. I.; Gudimenko, Y.; Ng, R.; Iskanderova, Z. A.; Grigorevski, A.; Kiseleva, L.; Edwards, D.; Finckenor, M. Surface Modification of Conductive and Nonconductive Paints for Space Durability Enhancement. *J. Spacecr. Rockets* **2006**, *43*, 443−450.

(12) Iskanderova, Z. A.; Kleiman, J. I.; Gudimenko, Y.; Tkachenko, A.; Tennyson, R. C.; Brown, I. G.; Monteiro, O. R. Metal Ion Implantation and Dynamic Ion Mixing for the Protection of High-Performance Polymers from Severe Oxidative Environment. *Nucl. Instrum. Methods Phys. Res., Sect. B* **1999**, *148*, 1090−1096.

(13) Gudimenko, Y.; Ng, R.; Kleiman, J.; Iskanderova, Z.; Milligan, D.; Tennyson, R. C.; Hughes, P. C. Enhancement of Space Durability of Materials and External Components Through Surface Modification. *J. Spacecr. Rockets* **2004**, *41*, 326−334.

(14) Brunsvold, A. L.; Minton, T. K.; Gouzman, I.; Grossman, E.; Gonzalez, R. An Investigation of the Resistance of Polyhedral Oligomeric Silsesquioxane Polyimide to Atomic-Oxygen Attack. *High Perform. Polym.* **2004**, *16*, 303−318.

(15) Verker, R.; Grossman, E.; Gouzman, I.; Eliaz, N. POSS-Polyimide Nanocomposite Films: Simulated Hypervelocity Space Debris and Atomic Oxygen Effects. *High Perform. Polym.* **2008**, *20*, 475−491.

(16) Minton, T. K.; Wright, M. E.; Tomczak, S. J.; Marquez, S. A.; Shen, L.; Brunsvold, A. L.; Cooper, R.; Zhang, J.; Vij, V.; Guenthner, A. J.; Petteys, B. J. Atomic Oxygen Effects on POSS Polyimides in Low Earth Orbit. *ACS Appl. Mater. Interfaces* **2012**, *4*, 492−502.

(17) Mikaelian, T. Spacecraft Charging and Hazards to Electronics in Space. *arXiv.org, e-Print Arch., Phys.* **2009**, 1−29.

(18) Watson, K. A.; Connell, J. W.; Delozier, D. M.; Smith, J. G., Jr. *Clear, Conductive, Transparent, Flexible Space Durable Composite Films for Electrostatic Charge Mitigation*. NASA Conf. Publ. 2004, 2004−213091; 8th Spacecraft Charging Technology Conference, 2003; pp 122−135.

(19) Robinson, P. A., Jr.; Coakley, P. Spacecraft Charging - Progress in the Study of Dielectrics and Plasmas. *IEEE Trans. Electr. Insul.* **1992**, *27*, 944−960.

(20) Smith, J. G., Jr; Connell, J. W.; Delozier, D. M.; Lillehei, P. T.; Watson, K. A.; Lin, Y.; Zhou, B.; Sun, Y. P. Space Durable Polymer/Carbon Nanotube Films for Electrostatic Charge Mitigation. *Polymer* **2004**, *45*, 825−836.

(21) Rutledge, S. K.; Mihelcic, J. A. Undercutting of Defects in Thin Film Protective Coatings on Polymer Surfaces Exposed to Atomic Oxygen. *Surf. Coat. Technol.* **1989**, *39−40*, 607−609.

(22) Herrero, J.; Guillén, C. Transparent Films on Polymers for Photovoltaic Applications. *Vacuum* **2002**, *67*, 611−616.

(23) Watson, K. A.; Ghose, S.; Delozier, D. M.; Smith, J. G., Jr; Connell, J. W. Transparent, Flexible, Conductive Carbon Nanotube Coatings for Electrostatic Charge Mitigation. *Polymer* **2005**, *46*, 2076−2085.

(24) Deki, S.; Aoi, Y.; Miyake, Y.; Gotoh, A.; Kajinami, A. Novel Wet Process For Preparation of Vanadium Oxide Thin Film. *MRS Bull.* **1996**, *31*, 1399−1406.

(25) Gouzman, I.; Girshevitz, O.; Grossman, E.; Eliaz, N.; Sukenik, C. N. Thin Film Oxide Barrier Layers: Protection of Kapton from Space Environment by Liquid Phase Deposition of Titanium Oxide. *ACS Appl. Mater. Interfaces* **2010**, *2*, 1835−1843.

(26) Saito, Y.; Sekiguchi, Y.; Mizuhata, M.; Deki, S. Continuous Deposition System of SnO_2 Thin Film by the Liquid Phase Deposition (LPD) Method. *J. Ceram. Soc. Jpn.* **2007**, *115*, 856−860.

(27) Cai, N.; Cho, J. Low Temperature Processed SnO_2 Films Using Aqueous Precursor Solutions. *Ceram. Int.* **2013**, *39*, 143−151.

(28) Kishioka, S.; Heineman, W. R. Electrochemical Liquid Phase Deposition of Tin Oxide on Gold Electrode. *Thin Solid Films* **2013**, *548*, 349−353.

(29) Razgon, A.; Sukenik, C. N. Ceramic Coatings for Fiber Matrix Composites: Titania Thin Films on Bismaleimide-Glass Fiber Composites. *J. Mater. Res.* **2005**, *20*, 2544−2552.

DOI: 10.1021/am5072817
ACS Appl. Mater. Interfaces 2015, 7, 3539−3546

(30) Pizem, H.; Gershevitz, O.; Goffer, Y.; Frimer, A. A.; Sukenik, C. N.; Sampathkumaran, U.; Milhet, X.; McIlwain, A.; De Guire, M. R.; Meador, M. A. B.; Sutter, J. K. Titania Deposition on PMR-15. *Chem. Mater.* **2005**, *17*, 3205−3213.
(31) ASTM D3359 - 09e2 Standard Test Methods for Measuring Adhesion by Tape Test; http://www.astm.org/Standards/D3359.htm.
(32) Briggs, D., Seah, M. P. *Practical Surface Analysis, Auger and X-Ray Photoelectron Spectroscopy*; John Wiley & Sons: Chichester, England, 1992; Vol *1*.
(33) Barradas, N. P.; Jeynes, C. Advanced Physics And Algorithms in the IBA Datafurnace. *Nucl. Instrum. Methods Phys. Res., Sect. B* **2008**, *266*, 1875−1879.
(34) Ziegler, J. F. SRIM-2003. *Nucl. Instrum. Methods Phys. Res., Sect. B* **2004**, *219−220*, 1027−1036.
(35) Sader, J. E.; Chon, J. W. M.; P, M. Calibration of Rectangular Atomic Force Microscope Cantilivers. *Rev. Sci. Instrum.* **1999**, *70*, 3967−3969.
(36) Shpilman, Z.; Gouzman, I.; Lempert, G.; Grossman, E.; Hoffman, A. Rf Plasma System as an Atomic Oxygen Exposure Facility. *Rev. Sci. Instrum.* **2008**, *79*, 025106/1−025106/6.
(37) De Groh, K. K.; Banks, B. A.; McCarthy, C. E.; Rucker, R. N.; Roberts, L. M.; Berger, L. A. MISSE 2 PEACE Polymers Atomic Oxygen Erosion Experiment on the International Space Station. *High Perform. Polym.* **2008**, *20*, 388−409.
(38) Du-Pont. Inc., Technical Bulletin, ″PYRALIN® Polyimide Coating PI 2545 PI 2540 Product Information″, 1993.
(39) Verker, R.; Grossman, E.; Eliaz, N. Erosion of Poss-Polyimide Films under Hypervelocity Impact and Atomic Oxygen: The Role of Mechanical Properties at Elevated Temperatures. *Acta Mater.* **2009**, *57*, 1112−1119.
(40) Wei-Kan, C. J. W. M. M.-A. N. *Backscatering Spectroscopy*; Academic Press, Inc: New York, 1978.
(41) Pizem, H.; Sukenik, C. N.; Sampathkumaran, U.; McIlwain, A. K.; De Guire, M. R. Effects of Substrate Surface Functionality on Solution-Deposited Titania Films. *Chem. Mater.* **2002**, *14*, 2476−2485.
(42) Gouzman, I.; Grossmann, E.; Murat, M.; Noter, Y.; Saar, N.; Zilberman, G.; Minton, T. K.; Garton, D. J.; Buczala, D.; Brunsvold, A. A Study of Atomic Oxygen Interactions with Protected Silver Surfaces. In *Proceedings of the 9th International Symposium on Materials in a Space Environment*; Fletcher, K., Ed.; European Space Agency, [Special Publication] SP, 2003; SP-540, pp 487−492.
(43) Laikhtman, A., Gouzman, I., Noter,Y., Grossman, E., Verker, R., Pippin, H. G. *Space Environment Effects on Fluorosilicone Rubber: In-Flight and Ground Simulation Experiments*. In The 10th International Symposium on Materials in a Space Environment & The 8th International Conference on Protection of Materilas and Stractures in a Space Environment Collioure, France, 2006.
(44) Minton, T. K.; Garton, D. J. Dynamics of Atomic-Oxygen-Induced Polymer Degradation in Low Earth Orbit. In *Advanced Series in Physical Chemistry: Chemical Dynamics in Extreme Environments*; World Scientific: Singapore, 2010; pp 420−489.
(45) Snyder, A.; Banks, B. A.; Waters, D. L. Undercutting Studies of Protected Kapton H Exposed to In-Space and Ground-Based Atomic Oxygen. *NASA/TM* **2006**, *i-iv*, 1−8.
(46) Gueymard, C. A. The Sun's Total and Spectral Irradiance for Solar Energy Applications and Solar Radiation Models. *Sol. Energy* **2004**, *76*, 423−453.
(47) http://www.goodfellow.com/E/Polyimide.html.
(48) Nonnenmacher, M.; O' Boyle, M. P.; Wickramasinghe, H. K. Kelvin Probe Force Microscopy. *Appl. Phys. Lett.* **1991**, *58*, 2921−2923.
(49) Ju, Y.; Wang, M.; Wang, Y.; Wang, S.; Fu, C. Electrical Properties of Amorphous Titanium Oxide Thin Films for Bolometric Application. *Adv. Condens. Matter Phys.* **2013**, 365475/1−365475/6.
(50) Breckenridge, R. G.; Hosler, W. R. Electrical Properties of Titanium Dioxide Semiconductors. *Phys. Rev.* **1953**, *91*, 793−802.
(51) Kojima, M.; Kato, H.; Imai, A.; Yoshida, A. Electronic Conduction of Tin Oxide Thin Films Prepared by Chemical Vapor Deposition. *J. Appl. Phys.* **1988**, *64*, 1902−1905.
(52) Serin, T.; Serin, N.; Karadeniz, S.; Sari, H.; Tugluoglu, N.; Pakma, O. Electrical, Structural and Optical Properties of SnO_2 Thin Films Prepared by Spray Pyrolysis. *J. Non-Cryst. Solids* **2006**, *352*, 209−215.
(53) Skelland, N. D. Rutherford Backscattering Spectroscopy of Insulating Materials. *Nucl. Instrum. Methods Phys. Res., Sect. B* **1994**, *84*, 361−367.
(54) Arafah, D. E.; Townsend, P. D. Changes in RBS Spectra from Surface Charge Effects. *Nucl. Instrum. Methods Phys. Res., Sect. B* **1984**, *232*, 399−400.
(55) Meyer, J. D.; Arafah, D. E. Influence of Electronic Charge Compensation on Rutherford Backscattering Spectra of Biased Insulators. *Nucl. Instrum. Methods Phys. Res., Sect. B* **1990**, *B50*, 109−113.
(56) Armstrong, J. C.; Mullendore, J. V.; Harris, W. R.; Marion, J. B. Equilibrium Charge-State Fractions of 0.2 to 6.5-Mev. Helium Ions In Carbon. *Proc. Phys. Soc., London* **1965**, *86*, 1283−1295.
(57) Dias, J. F.; Bulla, A.; Yoneama, M. L. Charging Effects in Thick Insulating Samples. *Nucl. Instrum. Methods Phys. Res., Sect. B* **2002**, *189*, 72−76.
(58) Gotlib-Vainshtein, K.; Girshevitz, O.; Sukenik, C. N.; Barlam, D.; Kalfon-Cohen, E.; Cohen, S. R. Oxide Surfaces with Tunable Stiffness. *J. Phys. Chem. C* **2013**, *117*, 22232−22239.
(59) http://www.ece.rochester.edu/~jones/demos/definitions.html.
(60) ESD Association Standard; http://www.esda.org/documents/ANSI-ESD_S541-2008.PDF.

DOI: 10.1021/am5072817
ACS Appl. Mater. Interfaces 2015, 7, 3539−3546